Ceramide-1-phosphate transfer protein enhances lipid transport by disrupting hydrophobic lipid–membrane contacts

Julia R. Rogers[1¤*] and Phillip L. Geissler[1,2†]

1 Department of Chemistry, University of California, Berkeley, CA, USA
2 Chemical Sciences Division, Lawrence Berkeley National Laboratory, Berkeley, CA, USA

¤Current Address: Department of Systems Biology, Columbia University, New York, NY, USA
†Deceased
* julia.rogers@berkeley.edu

Abstract

Cellular distributions of the sphingolipid ceramide-1-phosphate (C1P) impact essential biological processes. C1P levels are spatiotemporally regulated by ceramide-1-phosphate transfer protein (CPTP), which efficiently shuttles C1P between organelle membranes. Yet, how CPTP rapidly extracts and inserts C1P into a membrane remains unknown. Here, we devise a multiscale simulation approach to elucidate the biophysical details of CPTP-mediated C1P transport. We find that CPTP binds a membrane poised to extract and insert C1P and that membrane binding promotes conformational changes in CPTP that facilitate C1P uptake and release. By substantially disrupting a lipid's local hydrophobic environment in the membrane, CPTP lowers the activation free energy barrier for passive C1P desorption and enhances C1P extraction from the membrane. Upon uptake of C1P, further conformational changes may aid membrane unbinding in a manner reminiscent of the electrostatic switching mechanism used by other lipid transfer proteins. Most notably, we provide molecular evidence for CPTP's ability to catalyze C1P transport by breaking hydrophobic C1P–membrane contacts. Since this catalytic mechanism is biophysically related to that of passive lipid transport, it may be ubiquitously used by lipid transport proteins to rapidly traffic lipids between membranes and ensure membrane homeostasis.

Author summary

Critical cellular processes require spatiotemporal regulation of sphingolipid levels among organelle membranes. Programmed cell death and inflammation, for example, are impacted by the distribution of ceramide-1-phosphate (C1P). C1P levels are specifically altered by ceramide-1-phosphate transfer protein (CPTP), which mediates C1P intermembrane transport. Using a multiscale simulation approach tailored to studying lipid transport, we elucidate the molecular mechanism used by CPTP to rapidly transport C1P between membranes: Through conformational changes that are coupled to membrane binding, CPTP significantly disrupts C1P's local hydrophobic environment in a membrane and catalyzes its extraction. Not only is this catalytic mechanism biophysically similar to that of passive lipid transport, but it also shares molecular features with that of other lipid transfer proteins. Therefore, we suggest that

lipid transfer proteins may universally enhance lipid extraction by breaking hydrophobic lipid–membrane contacts. Our multiscale simulation approach offers a framework to efficiently test this hypothesis and, thus, further our molecular knowledge of how lipid transfer proteins function to regulate cellular lipid distributions.

Introduction

Sphingolipids play critical roles in numerous cellular processes, including cell growth, differentiation, migration, and survival [1, 2]. Normal biological function requires spatiotemporal regulation of sphingolipid levels among organelle membranes [2–4], and altered distributions are linked to the pathophysiology of diseases including cancers, inflammatory diseases, metabolic syndromes, and neurological disorders [1, 5–7]. Precise sphingolipid distributions are maintained through coordinated regulation of sphingolipid metabolism within specific organelle membranes and transport between them [3, 4, 8, 9]. While interorganelle transport can occur through vesicular trafficking [3, 9], individual sphingolipids are also specifically transported between membranes by lipid transfer proteins [9–14]. One such protein, ceramide-1-phosphate transfer protein (CPTP) transports ceramide-1-phosphate (C1P), a mitogenic and prosurvival sphingolipid [1, 15], from the *trans*-Golgi, where it is synthesized from ceramide, to nuclear and plasma membranes [16]. By selectively trafficking C1P from the *trans*-Golgi, CPTP modulates pro-inflammatory eicosanoid production, interluekin release, and autophagy, and, thus, may help reduce the risk for chronic inflammation [16–18].

Efforts to fully decipher and modulate CPTP's role in both homeostasis and disease, nevertheless, remain hampered by an incomplete biophysical understanding of how CPTP rapidly traffics C1P between organelles. Structural and biochemical studies [16, 19, 20] have elucidated initial details about how CPTP functions as a cytosolic lipid shuttle [11, 14]: During transit, CPTP houses C1P within a hydrophobic cavity at the interior of its all α-helical, sandwich-like structure [16], thereby shielding C1P's hydrophobic tails from unfavorable exposure to solvent. While this partially explains why CPTP facilitated transport of C1P is more rapid than passive transport, it fails to explain how CPTP swiftly extracts (and inserts) C1P from (into) a membrane. Based on crystallographic measurements, a cleft-like gating mechanism has been proposed to control access to CPTP's hydrophobic cavity and to facilitate C1P entry and exit [16]; however, because such molecular motions have yet to be resolved, their importance for C1P uptake and release is unclear. An additional puzzle is how CPTP overcomes the significant free energy barrier for lipid desorption from a membrane, which limits passive lipid transport rates [21–25]. We recently demonstrated that the activation free energy barrier for passive lipid desorption reflects the thermodynamic cost of breaking hydrophobic lipid–membrane contacts [25], and that it can be lowered by decreasing the hydrophobicity of the transferring lipid's local membrane environment [26]. Thus, we hypothesize that CPTP rapidly extracts C1P from a membrane by disrupting C1P–membrane hydrophobic contacts, thereby lowering the free energy barrier for lipid desorption and catalyzing C1P transport.

To test this hypothesis, we investigate how CPTP performs each individual step of the C1P transfer cycle using a multiscale molecular dynamics (MD) simulation approach. Significant structural differences between the apo and C1P-bound forms, observed in both published crystal structures [16] and our solution-phase simulations, indicate that conformational changes are required to accommodate C1P in CPTP's hydrophobic cavity. Consistent with previous results [16, 27], CPTP exhibits a single favorable membrane binding pose that aptly positions the entrance to its hydrophobic cavity at the membrane interface in our simulations. We find that membrane binding promotes rearrangements of CPTP's helices as expected for a cleft-like gating

mechanism to facilitate C1P entry and exit into its hydrophobic cavity. Key to CPTP's catalytic function, we find that the apo form substantially disrupts a lipid's local hydrophobic environment in the membrane. As a result, CPTP reduces the rate-limiting free energy barrier for C1P extraction. Uptake of C1P may then trigger conformational changes that prompt membrane unbinding and continuation of the transfer cycle. Overall, our simulations shed light on how CPTP rapidly traffics C1P between membranes and also offer molecular explanations for previous experimental findings. Significantly, our results provide the first evidence supporting the hypothesis that lipid transfer proteins universally catalyze lipid transport by breaking hydrophobic contacts between a target lipid and donor membrane.

Results

We use a multiscale simulation approach that builds upon previous structural studies [16, 27] and our earlier studies of passive lipid transport [25, 26] to efficiently and accurately characterize key elementary steps of C1P transport by CPTP. Specifically, we model the transport of C1P with a saturated, 16-carbon acyl chain, which is CPTP's most likely *in vivo* substrate [16], between membranes composed of 1-palmitoyl-2-oleoyl-*sn*-glycero-3-PC (POPC), which have been used in experimental transfer assays [19], by human CPTP. We use atomistic simulations to resolve conformational changes that occur upon membrane binding and to capture C1P extraction from and insertion into a membrane, whereas we use coarse-grained simulations to observe multiple membrane binding events, which require microsecond-long simulations. Using an enhanced sampling method specifically targeting the degrees of freedom that hinder passive lipid transport, we calculate an all-atom free energy profile of CPTP-mediated C1P extraction and compare it to that of passive C1P desorption from a membrane to assess CPTP's catalytic abilities.

CPTP's hydrophobic cavity must expand to accommodate C1P

CPTP has a two-layered, all α-helical topology that is homologous with the glycolipid transfer protein (GLTP) fold [18, 28–30]. Within the interior of CPTP's sandwich-like structure composed of nine α-helices is a hydrophobic cavity that adaptively expands to accommodate C1P. We first examined how the size of the cavity and overall structures of the apo and C1P-bound forms of CPTP differ in solution. To initialize solution-phase simulations, we used the most complete crystal structure of CPTP with C1P fully bound in its hydrophobic cavity (PDB 4K85). Final structures from our solution-phase simulations of the apo and C1P-bound forms are shown in Fig 1A-1C. Without C1P present in the cavity, CPTP's helices reorient themselves, closing off the entrance to the hydrophobic cavity and barring the entry of solvent molecules. In particular, helix $\alpha 2$, which is located on one side of CPTP's sandwich topology, and helices $\alpha 4$ and $\alpha 8$, which are located on the opposing side, angle into the hydrophobic cavity and fill the space otherwise occupied by C1P (Fig 1A). Due to the closer packing of multiple helices in the apo form, the hydrophobic cavity collapses (Fig 1B and 1C). To quantify the change in hydrophobic cavity volume, we use the geometry-based detection algorithm MDpocket [31] to identify the void between CPTP's two α-helical layers unoccupied by protein, and find that the total volume of the hydrophobic cavity in the apo form is on average only half the volume of the cavity in the C1P-bound form (Fig 1D). Consistent with conclusions made based on crystal structures [16], our results indicate that CPTP must undergo significant conformational changes to accommodate C1P in its hydrophobic cavity. Differences in the structures of the C1P-bound and apo forms in our simulations are further suggestive of the previously proposed cleft-like gating

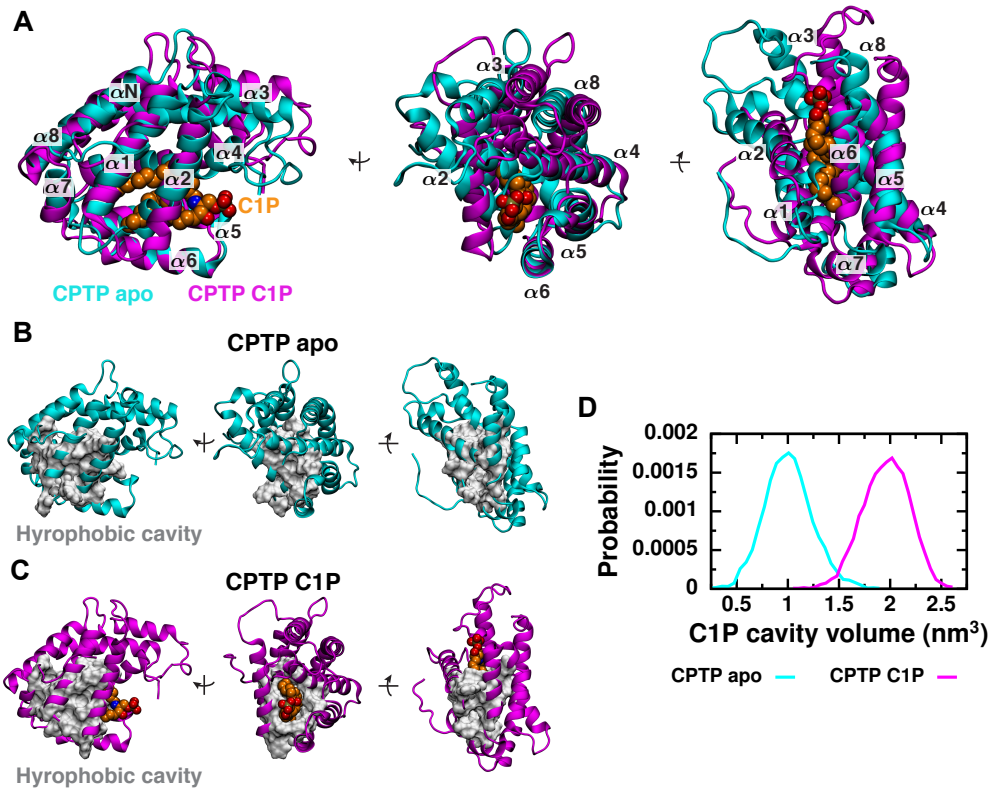

Fig 1. In solution, conformational differences between the apo and C1P-bound forms of CPTP tune the accessibility and volume of the hydrophobic cavity. (A) Superimposed structures of the apo form (cyan) and C1P-bound form (magenta) obtained from solution-phase simulations are shown from three views. Structures were aligned to minimize the root-mean-square deviation (RMSD) of Cα atoms of helix α6. Helices (αN and $\alpha 1 - \alpha 8$) are numbered from amino (N) to carboxy (C) termini. C1P is rendered as van der Waals spheres and colored orange. (B and C) Residues lining the hydrophobic cavity are shown as a gray surface on the (B) apo and (C) C1P-bound structures. (D) Distributions of the total volume of the hydrophobic cavity during solution-phase simulations of the apo and C1P-bound forms. Cavity volume is calculated as the volume of CPTP's interior unoccupied by protein heavy atoms using MDpocket [31] and includes volume occupied by C1P in the C1P-bound form.

mechanism [16]: To accomodate C1P, helices on one side of CPTP's sandwich-like structure are collectively displaced due to a substantial change in the location of helix α3, which connects residues on either side of the hydrophobic cavity (S1 Fig).

Membrane binding poises CPTP to extract C1P

We next characterized how CPTP, in both apo and C1P-bound forms, binds to a POPC membrane. To observe multiple spontaneous binding events, we performed coarse-grained simulations (S2 Fig). While the coarse-grained model accurately recapitulates the structure and internal dynamics of CPTP observed in our atomistic solution-phase simulations (S3 Fig and S4 Fig), it cannot capture conformational changes that may occur upon membrane binding. Thus, we converted membrane-bound, coarse-grained configurations back into all-atom representations in order to resolve

conformational changes that may result from CPTP–membrane interactions.

A single binding pose is observed in coarse-grained simulations (Fig 2 and S2 Fig), and CPTP remains favorably bound to the membrane in the same overall pose in all-atom simulations (Fig 2). This membrane-bound pose matches that predicted based

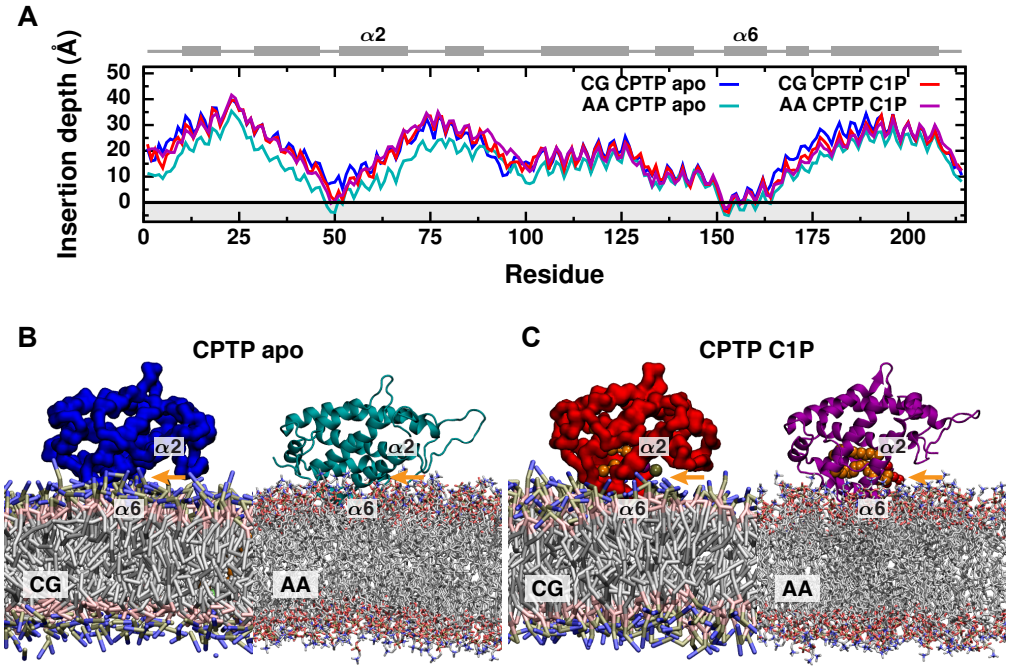

Fig 2. Both apo and C1P-bound forms of CPTP bind a membrane poised to extract or insert C1P. (A) Average insertion depth of each residue measured relative to the average position of lipid phosphate groups (black line) from coarse-grained (CG) and all-atom (AA) simulations. The gray region highlights the location of the membrane's hydrophobic core. CPTP's secondary structure is schematically illustrated above with helices represented as rectangles and unstructured loop regions as lines. (B and C) Representative configurations of the (B) apo form and (C) C1P-bound form of CPTP bound to a POPC membrane for both coarse-grained and all-atom representations. The entrance to CPTP's hydrophobic cavity is indicated with an orange arrow. C1P is rendered as van der Waals spheres and colored orange.

on CPTP's crystal structure modeled in the presence of an implicit membrane [16], which has previously been shown to be stable in all-atom MD simulations [27]. In both apo and C1P-bound forms, the loop connecting helices $\alpha1$ and $\alpha2$ along with helix $\alpha6$ inserts into the membrane's hydrophobic core (Fig 2A). A combination of hydrophobic and aromatic residues, specifically I49, F50, and F52 of the $\alpha1$-$\alpha2$ loop and W152, V153, and V160 of helix $\alpha6$, anchor CPTP to the membrane as predicted from crystal structures [16] and identified in previous simulations [27]. When bound to the membrane, the entrance to CPTP's hydrophobic cavity is aptly positioned at the membrane–solvent interface (Fig 2B and 2C). Additionally, the cleft between CPTP's two α-helical layers faces into the membrane's hydrophobic core, providing an avenue for C1P to move from the membrane into CPTP's hydrophobic cavity without exposing its tails to solvent.

Subtle differences in the binding pose of the apo form observed in all-atom versus coarse-grained representations (Fig 2A and 2B) suggest that conformational changes, which cannot be observed with the coarse-grained model, may be coupled to membrane

binding. Indeed, closer inspection of the all-atom simulations indicates that interactions with the membrane promote a widening of the entrance to CPTP's hydrophobic cavity. Helix $\alpha 2$, which partially gates the entrance to the hydrophobic cavity (Fig 1A), is rotated outward in membrane bound structures of both the apo and C1P-bound forms compared to their respective solution-phase structures (Fig 3A). We quantify this conformational change by the polar angle $\theta_{\alpha 2}$ and azimuthal angle $\phi_{\alpha 2}$ of helix $\alpha 2$ in a coordinate system defined by the membrane surface (Fig 3B and 3C). In order to calculate $\theta_{\alpha 2}$ and $\phi_{\alpha 2}$ for both solution-phase and membrane-bound structures, we use the plane that contains the top surface of helix $\alpha 6$ to approximate the plane of the membrane surface. We use helix $\alpha 6$ as an internal reference since helix $\alpha 6$ is approximately parallel to the membrane surface when CPTP is membrane bound (Fig 2) and has a rather rigid structure (S3 Fig and S4 Fig). A decrease in $\theta_{\alpha 2}$ indicates opening of the gate created by helix $\alpha 2$, whereas an increase in $\phi_{\alpha 2}$ indicates further opening. When C1P is bound, CPTP's cavity is expanded and the gate widened (highlighted by orange arrows in Fig 3A), resulting in increased $\theta_{\alpha 2}$ and decreased $\phi_{\alpha 2}$ compared to the apo form (Fig 3D). As shown in Fig 3D and S5 Fig A, membrane bound structures of CPTP have reduced $\theta_{\alpha 2}$, corresponding to more open gates, compared to their respective solution-phase structures on average. By locking down the gate created by helix $\alpha 2$ when in solution, the hydrophobic cavity, and any lipid inside, remains sealed off from solvent. Widening of the entrance to the hydrophobic cavity upon membrane binding (highlighted by gray arrows in Fig 3A) then readies CPTP to extract or insert C1P. As shown in Fig 3D and S5 Fig, the C1P-bound form of CPTP bound to the membrane has the smallest $\theta_{\alpha 2}$ and largest $\phi_{\alpha 2}$ on average. Such increased opening and flexibility of the helical gate upon membrane binding may further aid the release of C1P into the membrane.

Both the apo and C1P-bound forms of CPTP bind the membrane in the same overall pose and exhibit conformational changes of similar magnitude upon binding; however, such conformational changes enable the apo form to insert more deeply into the membrane's hydrophobic core (Fig 2). In the apo form, a slight widening of the entrance to the hydrophobic cavity brings helix $\alpha 2$ closer to the membrane surface. As a result, energetically favorable interactions between residues on helix $\alpha 2$ and the membrane are present in the apo form but not the C1P-bound form (Fig 4). In particular, two positively charged residues, R62 and R66, form significantly favorable electrostatic interactions with the membrane and anchor CPTP in its apo but not C1P-bound form. By anchoring helix $\alpha 2$ to the membrane, such favorable interactions may modulate the opening of the gate created by helix $\alpha 2$ in the apo form. Complete opening of the gate created by helix $\alpha 2$ to accommodate C1P inside CPTP's hydrophobic cavity breaks these favorable electrostatic interactions with the membrane and may thereby facilitate membrane unbinding after C1P uptake.

CPTP alters the membrane's physical properties to facilitate C1P extraction

When bound to the membrane, CPTP also influences the molecular structure and physical properties of the membrane. Previous simulations suggested that helix $\alpha 6$, in particular, can promote lipid reorientation into configurations apt for tail-first uptake by CPTP: By orienting lipids parallel with the membrane surface, the terminal carbons of their hydrophobic tails are positioned at the membrane surface and pointing into CPTP's hydrophobic cavity [27]. Consistent with this idea, we find that the hydrophobic tails of lipids in close proximity to both the apo and C1P-bound forms of CPTP are oriented more parallel to the membrane surface than expected for a POPC membrane without CPTP bound (Fig 5). In its apo form, CPTP promotes increased

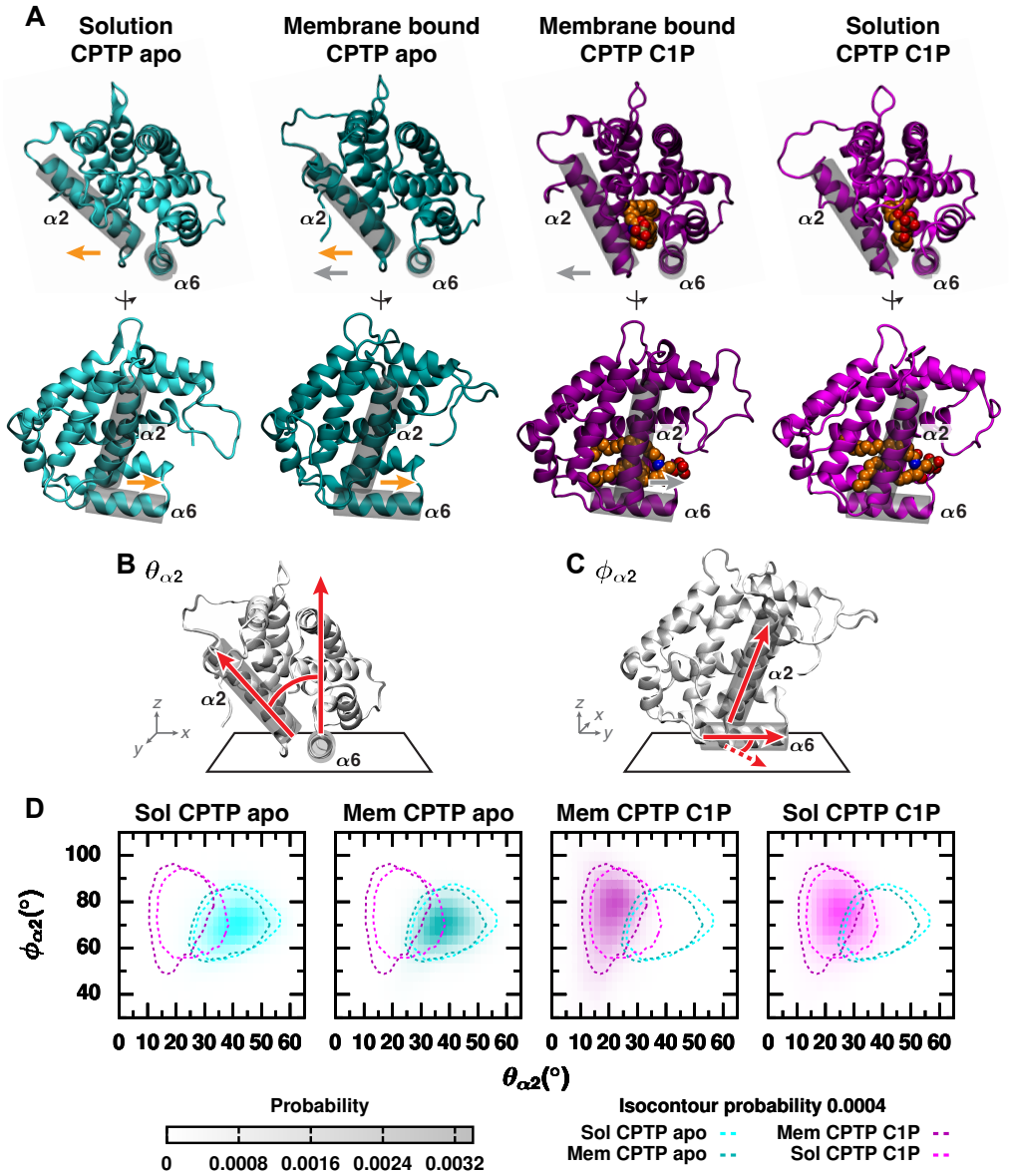

Fig 3. Conformational changes that promote the opening of gating helix $\alpha 2$ are coupled to membrane binding. (A) Orientation of helix $\alpha 2$ relative to helix $\alpha 6$ is highlighted on representative structures of both the apo and C1P-bound forms in both solution and bound to the membrane. Both helices are outlined by a gray cylinder. C1P is rendered as van der Waals spheres and colored orange. Orange arrows indicate gate opening upon C1P-binding to CPTP, and gray arrows indicate gate opening upon membrane binding. (B and C) Definitions of angles used to characterize gate opening. A coordinate system is defined by the plane containing helix $\alpha 6$, which nearly corresponds to the location of the membrane–solvent interface when CPTP is membrane bound. (B) $\theta_{\alpha 2}$ is the polar angle of helix $\alpha 2$ and (C) $\phi_{\alpha 2}$ is the azimuthal angle. The projection of the $\alpha 2$ vector onto the x-y plane is indicated with a dashed arrow. (D) Joint distributions of $\theta_{\alpha 2}$ and $\phi_{\alpha 2}$ from all-atom simulations of the apo and C1P-bound forms of CPTP both in solution and bound to the membrane. Isocontours for all systems are plotted atop each distribution for reference.

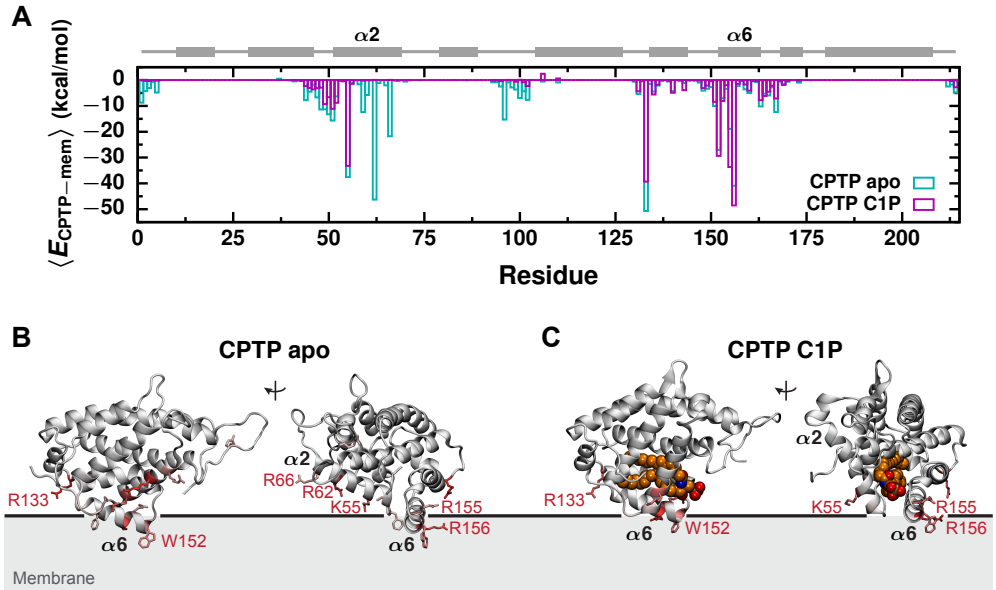

Fig 4. Favorable electrostatic interactions anchor the apo form deeply into the membrane. (A) Average interaction energy between each protein residue and the membrane, $\langle E_{\mathrm{CPTP-mem}} \rangle$, from all-atom simulations of the apo and C1P-bound forms of CPTP bound to a POPC membrane. CPTP's secondary structure is schematically illustrated above with helices represented as rectangles and unstructured loop regions as lines. (B and C) $\langle E_{\mathrm{CPTP-mem}} \rangle$ mapped onto the structures of the (B) apo and (C) C1P-bound forms of CPTP bound to the membrane. $\langle E_{\mathrm{CPTP-mem}} \rangle$ is indicated by the color of the residue. Residues that most favorably interact with the membrane are colored dark red, those that weakly or do not interact with the membrane are colored gray. Side chains of residues with $\langle E_{\mathrm{CPTP-mem}} \rangle < -12$ kcal/mol are rendered. Residues with $\langle E_{\mathrm{CPTP-mem}} \rangle < -18$ kcal/mol are labeled. C1P is rendered as van der Waals spheres and colored orange. The black line indicates the average position of phosphate groups of membrane lipids, and the membrane's hydrophobic core is shown in gray.

lipid reorientation necessary for C1P uptake. Around the C1P-bound form of CPTP, reorientation of membrane lipids may enable the formation of initial hydrophobic contacts between C1P and the membrane, helping to guide C1P from CPTP's hydrophobic cavity into the membrane.

Another membrane property that is especially key to lipid transport is the hydrophobicity of a lipid's local membrane environment. We previously demonstrated that the activation free energy for passive lipid transport correlates with the average number of hydrophobic contacts a lipid makes with surrounding membrane lipids, $\langle n_{\mathrm{CC}} \rangle_{\mathrm{mem}}$ [26]. As $\langle n_{\mathrm{CC}} \rangle_{\mathrm{mem}}$ decreases, the rate of passive lipid desorption from a membrane increases [26]. Fig 6 demonstrates how the apo and C1P-bound forms of CPTP impact $\langle n_{\mathrm{CC}} \rangle_{\mathrm{mem}}$. The C1P-bound form only minimally reduces the number of hydrophobic contacts that nearby lipids make with other membrane lipids. In contrast, the apo form significantly disrupts the hydrophobic environment of nearby lipids: Lipids within 1 nm of its binding location make on average 1,950 hydrophobic contacts with other membrane lipids (Fig 6B), whereas when CPTP is not bound to the membrane, POPC lipids form an average of 2,330 contacts with each other [26]. Based on the relationship between $\langle n_{\mathrm{CC}} \rangle_{\mathrm{mem}}$ and the free energy barrier for passive lipid desorption provided in [26], this reduction in $\langle n_{\mathrm{CC}} \rangle_{\mathrm{mem}}$ by 380 contacts corresponds to an expected decrease in the free energy barrier of 2.2 kcal/mol. Thus, the apo form of CPTP may

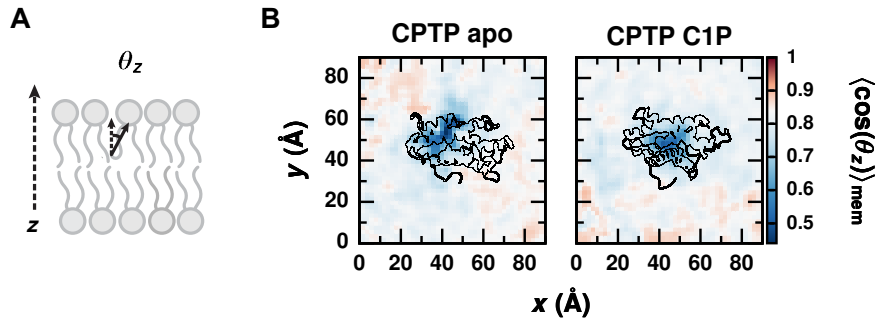

Fig 5. CPTP reorients nearby lipids in the membrane. (A) Lipid orientation is characterized by the angle θ_z each lipid tail makes with the z axis, which is normal to the membrane surface. (B) Average $\cos(\theta_z)$ of membrane lipids as a function of a lipid's displacement in the xy plane from CPTP. Color scale is set relative to $\langle \cos(\theta_z) \rangle_{\text{mem}}$ for a POPC membrane in the absence of CPTP; membrane regions where lipids are oriented more perpendicular to the membrane surface are colored red, and regions where lipids are more parallel to the membrane surface are colored blue. The structures of the apo and C1P-bound forms of CPTP bound to the membrane are outlined for reference.

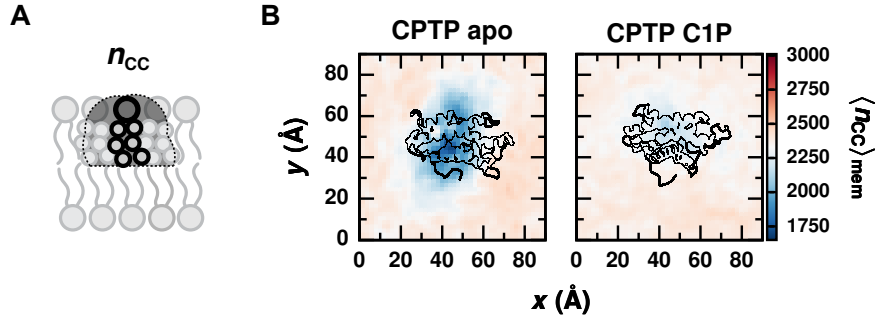

Fig 6. The apo form of CPTP significantly disrupts the local hydrophobic membrane environment of lipids below. (A) A lipid's hydrophobic environment is characterized by the number of hydrophobic carbon–carbon contacts it makes with surrounding lipids, n_{CC}. (B) Average n_{CC} of membrane lipids as a function of a lipid's displacement in the xy plane from CPTP. Color scale is set relative to $\langle n_{\text{CC}} \rangle_{\text{mem}}$ for a POPC membrane in the absence of CPTP; membrane regions where lipids make more contacts than an unperturbed POPC membrane are colored red, and regions where lipids make less are colored blue. The structures of the apo and C1P-bound forms of CPTP bound to the membrane are outlined for reference.

rapidly extract C1P by reducing the barrier for hydrophobic C1P–membrane contact breakage, which limits the rate of passive lipid transport.

CPTP rapidly extracts C1P by lowering the free energy barrier for breaking hydrophobic C1P–membrane contacts

To determine if CPTP lowers the free energy barrier for hydrophobic C1P–membrane contact breakage, we performed all-atom free energy calculations. Specifically, we calculated the free energy landscape along two coordinates expected to capture key intermediates of CPTP facilitated C1P transport: (1) The reaction coordinate for passive lipid (L) transport via solvent (xS), r_{LxS}, defined in [25] and Eq 1 in the

Methods, describes interactions between C1P and the membrane. r_{LxS} monitors progress from configurations with C1P in the membrane (which exhibit many hydrophobic lipid–membrane contacts and large values of r_{LxS}) to configurations with the lipid outside the membrane (which lack hydrophobic lipid–membrane contacts and have negative values of r_{LxS}) [25, 26]. (2) The fraction of contacts C1P makes with CPTP when fully inside its hydrophobic cavity, Q, monitors progress from configurations with C1P outside CPTP (which have values of Q close to zero) to configurations with C1P inside CPTP (which have values of Q close to one). Q is calculated using the functional form developed to calculate the fraction of native protein contacts and defined in Eq 4 in the Methods [32]. CPTP–C1P contact pairs used to calculate Q include: (a) hydrophobic contacts between C1P and residues that line CPTP's hydrophobic cavity and (b) polar contacts between C1P's headgroup and sphingoid backbone that are responsible for C1P recognition. (A triad of cationic residues located within a positively-charged surface pocket at the entrance to the hydrophobic cavity specifically engage C1P's phosphate headgroup, and a bifurcated hydrogen bond recognizes C1P's acyl-amide moiety [16].) To efficiently calculate this free energy landscape, we performed multi-walker [33] well-tempered metadynamics simulations [34] in which walkers were initiated from both apo and C1P-bound forms of CPTP bound to the membrane. This facilitated sampling of both forward and reverse transitions between configurations with C1P in the membrane and configurations with C1P inside CPTP, and convergence, assessed using the time-independent estimator of Tiwary and Parrinello [35], was obtained after 500 ns (cumulatively 10 μs) (S6 Fig).

The free energy landscape along r_{LxS} and Q is shown in Fig 7A. At the global free energy minimum (outlined in cyan in Fig 7A), C1P resides in the membrane where it makes many hydrophobic contacts with surrounding membrane lipids but does not substantially interact with CPTP. An example of a configuration found within the global free energy minimum is shown in Fig 7D1. At the second most favorable minimum in the free energy landscape (outlined in magenta in Fig 7A), C1P resides within CPTP's hydrophobic cavity but does not form hydrophobic contacts with membrane lipids. An example of a configuration found at this local minimum is shown in Fig 7D12. This free energy profile is consistent with CPTP's observed function as a C1P transporter: CPTP serves as a free energetically favorable vehicle for C1P transport between even more favorable states in which C1P is part of a membrane.

Fig 7B shows free energy profiles along r_{LxS} both in the presence and absence of CPTP. The free energy profiles match at large values of r_{LxS} as expected – being a catalyst, CPTP does not alter the relative probability of configurations within the global free energy minimum around $r_{\mathrm{LxS}} \approx 11.8$. The free energy profile for passive C1P transport exhibits a rate-limiting activation free energy barrier of 15.46 ± 0.08 kcal/mol at $r_{\mathrm{LxS}} \approx 0$. When CPTP is present, the free energy barrier for C1P desorption from the membrane is reduced to 13.0 ± 0.2 kcal/mol and shifted to slightly larger values of r_{LxS}. CPTP lowers the free energy barrier by 2.5 ± 0.2 kcal/mol, corresponding to almost a 100 fold speedup in the rate of lipid transport at room temperature. Furthermore, this value is in agreement with the one predicted in the previous section based on the maximal reduction in $\langle n_{\mathrm{CC}} \rangle_{\mathrm{mem}}$ caused by the apo form. By disrupting C1P's local hydrophobic environment in the membrane (Fig 6), CPTP lowers the free energy barrier that limits the rate of C1P desorption from a membrane and, thus, catalyzes lipid extraction. Because CPTP provides C1P with another favorable hydrophobic environment, C1P enters CPTP's hydrophobic cavity after fewer hydrophobic contacts with the membrane have been broken than as required for C1P desorption into solvent, which offers no favorable hydrophobic environment. As a result, the free energy barrier for lipid desorption is shifted to slightly larger values of r_{LxS} when CPTP is present. Indeed, as illustrated by an example configuration near this free

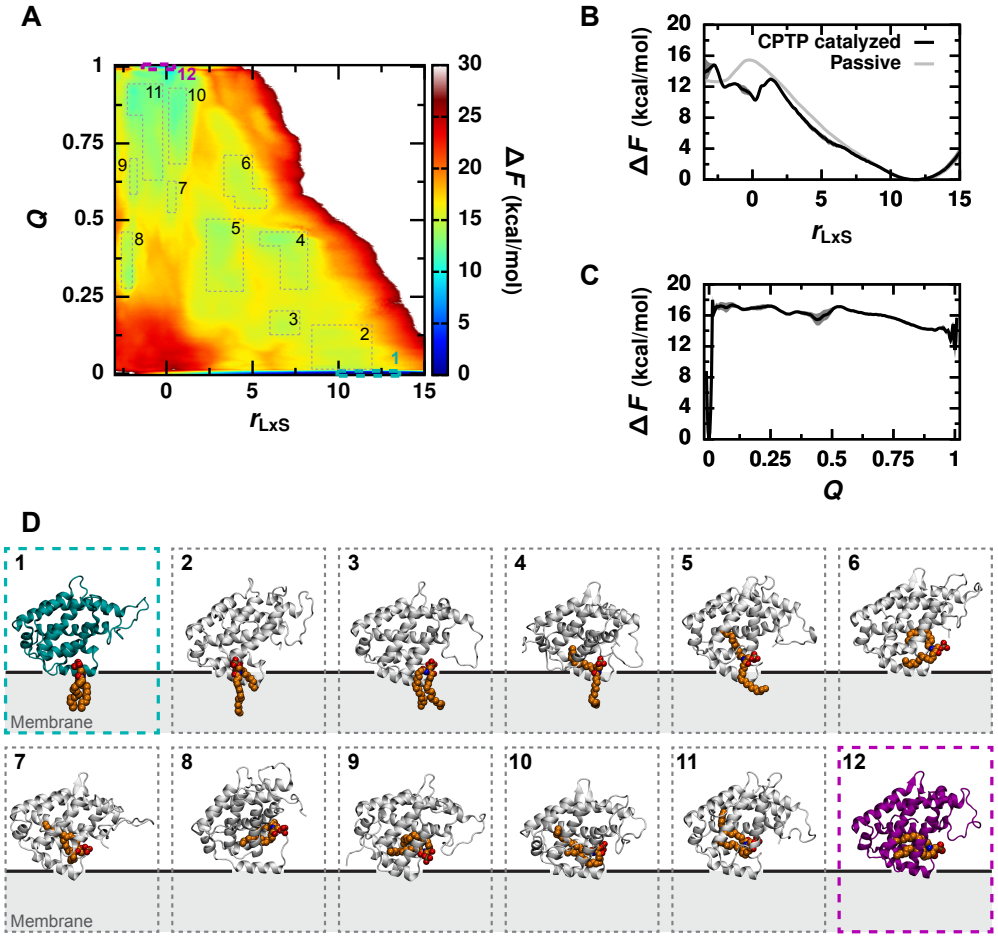

Fig 7. CPTP lowers the free energy barrier for hydrophobic C1P–membrane contact breakage. (A) Free energy landscape along r_{LxS} and Q. (B and C) Free energy profiles along (B) r_{LxS} or (C) Q obtained from the free energy landscape in (A). Error bars indicate standard error computed with block averaging. In (B), the free energy profile along r_{LxS} for passive C1P transfer is also shown; error is comparable to the line width. (D) Example configurations from different regions of the free energy landscape outlined in (A). C1P is rendered as van der Waals spheres and colored orange. The apo form of CPTP in configuration 1 is colored dark cyan, and the C1P-bound form in configuration 12 is colored dark magenta. The black line indicates the average position of phosphate groups of membrane lipids, and the membrane's hydrophobic core is shown in gray. Corresponding views looking into the hydrophobic cavity are shown in S7 Fig.

energy barrier in Fig 7D5, C1P maintains hydrophobic contacts with the membrane while also forming contacts with CPTP.

The free energy profile along Q (Fig 7C) suggests that C1P entry into CPTP's hydrophobic cavity may require passage through multiple metastable intermediates. Configurations representative of potential intermediates are shown in Fig 7D and S7 Fig. Configurations 2 and 3 shown in Fig 7D and S7 Fig illustrate how interactions with helices $\alpha 6$ and $\alpha 2$ can position C1P for tail-first entry into CPTP's hydrophobic cavity. Based on the observation of two C1P-binding modes in crystal structures, C1P entry and exit have been suggested to occur through a two-step mechanism whereby the acyl

chain enters into the cavity before the sphingosine during entry and leaves after the sphingosine during exit [16]. Consistent with this, we observe configurations with one tail of C1P inside CPTP's hydrophobic cavity and the other still within the membrane (configurations 4 and 5 in Fig 7D and S7 Fig). We do not observe a preference for one tail over the other to be housed within the cavity. For example, the acyl chain is found in the cavity in configurations 5 and 6 shown in Fig 7D and S7 Fig, whereas the sphingosine chain is found in the cavity in configurations 2, 4, and 8. Nevertheless, our findings support a two-step mechanism whereby each tail of C1P enters into and exits from CPTP's hydrophobic cavity individually. Once C1P has fully broken hydrophobic contacts with the membrane, it can adopt various configurations inside CPTP's hydrophobic cavity as illustrated by configurations 9-12 in Fig 7D and S7 Fig. Collectively, the intermediates observed in our simulations suggest that CPTP may extract C1P through multiple, molecularly diverse mechanisms.

Discussion

Cytosolic shuttle-like lipid transfer proteins enable rapid alteration of membrane compositions through trafficking of individual lipids [10–14]. Yet, how they swiftly extract individual lipids from a membrane remains an outstanding question. Our recent discovery that the rate of passive lipid exchange is limited by the disruption of a lipid's local hydrophobic environment [25, 26] suggests that lipid transfer proteins may catalyze lipid extraction by lowering the free energy barrier for hydrophobic lipid–membrane contact breakage. Here, we specifically tested this hypothesis by investigating how CPTP transports the bioactive sphingolipid C1P using a consecutive multiscale simulation scheme tailored to studying lipid transport via lipid transfer proteins: We used coarse-grained MD simulations to observe multiple spontaneous membrane binding events, which occur over microsecond timescales, and then used all-atom MD simulations to resolve key conformational changes that facilitate C1P uptake and to quantify CPTP's ability to catalyze C1P extraction from a membrane. Such consecutive multiscale schemes are ideal for studying process whose elementary steps occur at varied time and length scales, such as lipid transfer cycles. Indeed, a similar approach was recently used to investigate influenza hemagglutinin driven membrane fusion [36], a process related to vesicular lipid transport [12, 37].

Based on our simulations, we propose a molecular mechanism for how CPTP functions as a cytosolic C1P shuttle that is consistent with the previously suggested cleft-like gating mechanism [16]: To initiate a transfer event, the apo form of CPTP, whose collapsed hydrophobic cavity is closed off to C1P entry, binds a donor membrane. Interactions between the membrane and helix $\alpha 6$ in addition to gating helix $\alpha 2$ anchor CPTP deeply into the membrane and aptly position the entrance to its hydrophobic cavity at the membrane–solvent interface. Strong electrostatic interactions between positively charged residues on gating helix $\alpha 2$ facilitate cleft widening and gate opening. Poised for C1P entry into its hydrophobic cavity, CPTP significantly disrupts C1P's local hydrophobic membrane environment. This lowers the free energy barrier for C1P extraction from the membrane and enables CPTP to catalyze C1P transport. Additionally, interactions between C1P and residues on helices $\alpha 2$ and $\alpha 6$ orient C1P for tail-first uptake into CPTP's hydrophobic cavity. Entry proceeds through a two-step mechanism in which one tail of C1P enters prior to the other. Complete uptake of C1P into CPTP's hydrophobic cavity further opens gating helix $\alpha 2$. Such conformational changes break strong electrostatic interactions with the membrane that had previously anchored the apo form, potentially facilitating membrane unbinding. Having extracted C1P from a donor membrane, CPTP then proceeds to insert C1P into an acceptor membrane, a free energetically downhill event, to complete a transfer cycle.

Our proposed mechanism offers new hypotheses for how certain anionic lipids may enhance C1P transfer by CPTP. Including PS, PI(4,5)P_2, or PI4P, but not other anionic lipids, in donor membranes has been shown to enhance C1P transport in *in vitro* assays [19, 20]. Through specific interactions with CPTP's helix $\alpha 6$ and $\alpha 3 - \alpha 4$ loop, these lipids may help position the entrance to CPTP's hydrophobic cavity at the membrane surface and regulate its activity [19, 20, 27]. We hypothesize that PS, PI(4,5)P_2, and PI4P may also interact with arginine and lysine residues on helix $\alpha 2$ when CPTP is bound to the membrane in its apo form. Compared to other anionic lipids, PS, PI(4,5)P_2, and PI4P have larger headgroups with terminal acidic groups that may allow them to interact with these basic residues on helix $\alpha 2$, which are located farther above the membrane surface than residues on helix $\alpha 6$. Such interactions may facilitate binding of the apo form to the membrane and also promote opening of gating helix $\alpha 2$ and widening of CPTP's hydrophobic cavity as necessary for C1P uptake.

Our proposed mechanism for C1P transfer via CPTP additionally shares similarities to mechanisms of other cytosolic shuttle-like lipid transfer proteins, despite differences in their structures and lipid specificities. For example, members of the StARkin (relatives (kin) of steroidogenic acute regulatory protein (StAR)) superfamily, which have α-β topologies and bind phospholipids in the opposite orientation to CPTP (head-first versus tail-first) [14, 38], also undergo conformational changes upon membrane binding that facilitate opening of their hydrophobic cavities [39–43]. Lipid transfer proteins in the Sec14 and oxysterol-binding protein (OSBP)-related protein (ORP) families, which have well-defined lids to their hydrophobic cavities and bind phospholipids tail-first [14, 38], similarly exhibit conformational changes upon membrane binding that displace the lids to their hydrophobic cavities as required for lipid uptake [44–46]. Thus, our results add to the growing evidence that lipid transfer proteins couple conformational changes to membrane binding to rapidly traffic lipids.

Electrostatic interactions between basic protein residues and anionic lipids can promote the aforementioned conformational changes in other lipid transfer proteins and aid lipid uptake [40, 44, 45]. Similarly, we identify a potential role for electrostatic interactions in facilitating opening of CPTP's gating helix $\alpha 2$. Complete opening of this gate to accommodate C1P inside CPTP's hydrophobic cavity breaks these favorable electrostatic interactions. This may enable membrane unbinding in a manner reminiscent of the electrostatic switching mechanism used by Osh6p, a member of the ORP family that has a well-defined lid to its hydrophobic cavity [46]. Such switching mechanisms, in which a lipid transfer protein's membrane affinity depends on lipid occupancy, enable efficient transfer cycles by ensuring membrane binding is transient [46, 47].

Significantly, we demonstrate how CPTP enhances the rate of C1P transport by breaking hydrophobic C1P–membrane contacts and lowering the activation free energy barrier for lipid extraction. To our knowledge, this offers the first molecular evidence that a lipid transfer protein catalyzes lipid extraction from a membrane. Because the catalytic mechanism described here is closely related to that of passive lipid transport [25, 26], we suspect it may be generally used by lipid transfer proteins, not just CPTP, to increase the rate of lipid transport between cell membranes. For example, the sterol transfer protein StarD4 has been shown to deform donor membranes [48], as one would expect for a protein that catalyzes lipid transfer by disrupting a lipid's local hydrophobic environment [26]. Our mulitscale simulation approach provides a framework to efficiently test this hypothesis and, thus, advance our understanding of how lipid transfer proteins rapidly traffic lipids to ensure membrane homeostasis.

Methods

Molecular dynamics simulations

We performed molecular dynamics simulations of CPTP both in solution and in the presence of a POPC membrane at both all-atom and coarse-grained resolutions using GROMACS 2019 [49]. The CHARMM36 force field [50] in combination with the CHARMM TIP3P water model [51] was used for the all-atom simulations. CHARMM36 force field parameters developed for sphingolipids [52] were used for C1P with a saturated acyl chain of 16 carbons (16:0-C1P). The MARTINI 2.3P force field [53] in combination with polarizable MARTINI water model [54] was used for all coarse-grained simulations since it accurately reproduces the binding poses of peripheral membrane proteins [53]. An ElNeDyn elastic network [55] with harmonic springs connecting all backbone beads within 0.9 nm of each other and a spring constant of 500 kJ/mol/nm^2 was used to maintain the overall shape of CPTP in its apo and C1P-bound forms. Parameters for 16:0-C1P were chosen according to the standard MARTINI 2.0 lipid definitions and building block rules [56].

All-atom solution-phase simulations

The crystal structure of CPTP provided in PDB 4K85 [16] was used to initialize all-atom simulations since it has the most residues fully resolved out of all structures of CPTP with C1P fully bound. The first six N-terminal residues that were not resolved in PDB 4K85 were built using MODELLER [57, 58]. To investigate the transfer of CPTP's most likely *in vivo* substrate, the structure of 16:0-C1P fully bound inside CPTP provided in PDB 4K84 was aligned onto the structure of C1P with a saturated acyl chain of 12 carbons (12:0-C1P) present in PDB 4K85 to generate an initial configuration of CPTP in its C1P-bound form. C1P was removed from this structure to generate an initial configuration of the apo form. Both initial structures of the apo and C1P-bound forms were solvated in triclinic boxes of pre-equilibrated water molecules with dimensions chosen such that the minimum distance between any protein atom and the box walls was at least 2 nm. Sodium and chloride ions were added to achieve a salt concentration of 150 mM, matching the conditions used in *in vitro* experiments of C1P transfer by CPTP [19], and to fully neutralize each system. Both systems were then energy minimized using the steepest descent algorithm and equilibirated using a three-step protocol: (1) a 200 ps simulation in an isothermal–isochoric (NVT) ensemble with the positions of CPTP's heavy atoms restrained by harmonic potentials with a force constant of 1000 kJ/mol/nm^2 to equilibrate the solvent molecules and adjust the system density; (2) a 200 ps simulation in an isothermal–isobaric (NPT) ensemble using the Berendsen barostat [59] to maintain the pressure with isotropic pressure coupling and a coupling time constant of 2 ps; and (3) a 200 ps simulation in an NPT ensemble using the Parinello-Rahman barostat [60] with a coupling time constant of 5 ps. Subsequently, production simulations in an NPT ensemble were run for 300 ns using the parameters given below. The final 200 ns of each of these simulations was analyzed to characterize the solution-phase structure of the apo and C1P-bound forms of CPTP. The final configurations from these simulations were used to initialize simulations with a POPC bilayer present.

Coarse-grained simulations of CPTP in the presence of a membrane

Coarse-grained bilayers of 264 lipids surrounded by 3.2 nm slabs of solvent were built using INSANE [61] for simulations of CPTP in the presence of a membrane. For simulations of the apo form, the bilayer consisted of 262 POPC lipids and two 16:0-C1P lipids, one in each leaflet. For simulations of the C1P-bound form, the bilayer consisted

of 264 POPC lipids. Prior to the addition of CPTP into the solvent surrounding the bilayer, the structures of both bilayers were fully relaxed from their initial lattice configurations. This involved an energy minimization using the steepest descent algorithm followed by equilibration using a two-step protocol: (1) a 500 ps simulation using a 10 fs time step and the Berendsen barostat [59] with semi-isotropic presssure coupling and a coupling time constant of 3 ps; and (2) a 1 ns simulation using a 20 ps time step and the Parinello-Rahman barostat [60] with a coupling time constant of 12 ps. Subsequently, a 50 ns production run was performed to obtain bilayer structures that were used to construct initial configurations of CPTP in the presence of a membrane.

The martinize.py script [62] was used to construct coarse-grained protein topologies and structures based on the final configurations of the apo and C1P-bound forms of CPTP obtained from all-atom solution-phase simulations. Both coarse-grained structures were then fully equilibrated in solution through an energy minimization and a three-step protocol: (1) a 500 ps simulation in an NVT ensemble using a 10 fs time step and with the positions of CPTP's backbone beads restrained by harmonic potentials with a force constant of 1000 kJ/mol/nm^2 to equilibrate solvent molecules and adjust the system density; (2) a 500 ps simulation in an NPT ensemble using a 20 fs time step and the Berendsen barostat [59] with isotropic pressure coupling and a coupling time constant of 3 ps; and (3) a 500 ps simulation using a 20 fs time step and the Parinello-Rahman barostat [60] with a coupling time constant of 12 ps. Subsequently, 300 ns production runs were performed to obtain structures of CPTP used to initialize simulations that probe membrane binding.

For simulations of both forms of CPTP in the presence of a membrane, four different initial coarse-grained configurations were built by inserting a structure of CPTP sampled during the last 100 ns of the coarse-grained solution-phase simulation in a random location and orientation in the solvent around the equilibrated bilayer such that the minimum distance between any atom of CPTP and the membrane was 6 Å. Each replicate was then energy minimized and equilibrated using a three-step protocol: (1) a 500 ps simulation in an NVT ensemble using a 10 fs time step and with the positions of CPTP's backbone beads restrained by harmonic potentials with a force constant of 1000 kJ/mol/nm^2 to equilibrate solvent molecules and adjust the system density; (2) a 500 ps simulation in an NPT ensemble using a 20 fs time step and the Berendsen barostat [59] with semi-isotropic pressure coupling and a coupling time constant of 3 ps; and (3) a 1 ns simulation using a 20 fs time step and the Parinello-Rahman barostat [60] with a coupling time constant of 12 ps. During production runs of 2 μs, CPTP spontaneously bound to the membrane in all but one replicate of the apo form (S2 Fig), which was excluded from analysis of CPTP's membrane binding pose in coarse-grained simulations.

All-atom simulations of CPTP bound to a membrane

Membrane bound coarse-grained configurations of the apo and C1P-bound forms of CPTP were then backmapped into all-atom representations using the backward method [63]. The systems then underwent a three-step equilibration using the same protocol as used for the all-atom solution-phase simulations but with semi-isotropic pressure coupling. Subsequently, 300 ns production runs were performed. The final 200 ns from each of these runs was used to analyze all-atom configurations of CPTP bound to a membrane.

All-atom production simulation parameters

All simulations were performed in an NPT ensemble at a pressure of 1 bar and temperature of 310 K. Separate Nosé-Hoover thermostats [64, 65] were used for the solvent and solute molecules. The pressure was maintained using the Parinello-Rahman

barostat [60] with a compressibility of 4.5×10^{-5} bar^{-1} and coupling time constant of 1 ps. Isotropic pressure coupling was used in solution-phase simulations, and semi-isotropic coupling was used in simulations with a bilayer. Dynamics were evolved using the leapfrog algorithm [66] and a 2 fs time step. All bonds to hydrogen were constrained using the LINCS algorithm [67]. Lennard-Jones forces were smoothly switched off between 0.8 and 1.2 nm. Real-space Coulomb interactions were truncated at 1.2 nm, and long-ranged Coulomb interactions were calculated using Particle Mesh Ewald (PME) summation [68]. Neighbor lists were constructed using the Verlet list cut-off scheme [69].

Coarse-grained production simulation parameters

All simulations were performed in an NPT ensemble at a pressure of 1 bar and temperature of 310 K. To avoid the "hot solvent–cold solvent" problem [70], separate V-rescale thermostats [71] were used for the solvent and solute molecules. The pressure was maintained using the Parinello-Rahman barostat [60] with a compressibility of 3×10^{-4} bar^{-1} and coupling time constant of 12 ps. Isotropic pressure coupling was used in solution-phase simulations, and semi-isotropic coupling was used in simulations with a bilayer. Dynamics were evolved using the leapfrog algorithm [66] and a 20 fs time step. Lennard-Jones and Coulomb interactions were truncated at 1.1 nm, and long-ranged Coulomb interactions were calculated using PME summation [68]. A relative dielectric constant of 2.5 was used. Neighbor lists were constructed using the Verlet list cut-off scheme [69].

Analysis of CPTP's structure and interactions with the membrane

We analyzed the structure of apo and C1P-bound forms of CPTP both in solution and bound to a membrane. Analysis was performed using a combination of MDAnalysis [72] and NumPy [73] Python libraries in addition to GROMACS tools [49] and MDpocket [31].

Hydrophobic cavity volume

We quantified the volume of CPTP's hydrophobic cavity using MDpocket [31]. Only protein atoms were considered for this analysis. First, simulation frames were aligned to a common reference, specifically the Cα atoms of residues $10 - 208$ of the last frame of the solution-phase simulation of the C1P-bound form of C1P. This selection of residues excludes the flexible, unstructured termini. Then, the region at the interior of CPTP unoccupied by protein heavy atoms during at least 20% of the solution-phase simulation of the C1P-bound form was identified for analysis. The volume unoccupied in this region during solution-phase simulations of both the apo and C1P-bound forms was used as a measure of hydrophobic cavity volume.

Insertion depth

The insertion depth of each residue was calculated as the average signed distance in z, which is the axis normal to the membrane, between the center of mass (COM) of each residue and the average position of phosphate atoms (beads) in all-atom (coarse-grained) simulations.

Orientation of gating helix $\alpha 2$

To calculate the angles $\theta_{\alpha 2}$ and $\phi_{\alpha 2}$ (Fig 3B-C), the Cα atoms of residues 54 and 65 were used to define the vector along the axis of helix $\alpha 2$, and an internal coordinate system was defined by the plane containing helix $\alpha 6$. The Cα atoms of residues 155, 158, and 162 were used to define the plane that contains the top surface of helix $\alpha 6$ when CPTP is membrane bound. $\theta_{\alpha 2}$ and $\phi_{\alpha 2}$ are the polar and azimuthal angles, respectively, of the $\alpha 2$ vector in this internal coordinate system. $\phi_{\alpha 2}$ was specifically calculated as the angle between the projection of the $\alpha 2$ vector onto the plane and the vector along the axis of helix $\alpha 6$ defined by the Cα atoms of residues 155 and 162.

CPTP–membrane interaction energy

The interaction energy between each residue of CPTP and the membrane, $E_{\mathrm{CPTP-mem}}$, was calculated as the sum of short-ranged Lennard-Jones and Coulomb interaction energy terms between each residue and the membrane.

Lipid tail orientation

The orientation of each lipid tail was quantified by the angle θ_z (Fig 5A) between the z axis, which is normal to the membrane surface on average, and the vector connecting the terminal carbon of each tail to atom C2 for POPC or to atom C2S for C1P.

Number of hydrophobic contacts between lipids

The number of hydrophobic contacts between lipids, n_{CC}, (Fig 6A) was calculated based on the distances $d_{\mathrm{CC}}^{(i)}$ between hydrophobic carbons of two different lipids, where i labels a particular carbon-carbon (CC) pair. For all-atom POPC lipids, hydrophobic carbons include atoms C23−C216 and C33−C316. For all-atom C1P, hydrophobic carbons include atoms C3F−C16F and C5S−C18S. n_{CC} is the number of CC pairs that satisfy $d_{\mathrm{CC}}^{(i)} \leq 1$ nm.

Free energy calculations

CPTP catalyzed C1P transport

We calculated free energy landscapes along the reaction coordinate for passive lipid transport, r_{LxS}, and fraction of contacts between C1P and CPTP, Q. As determined in [25], r_{LxS} is a linear combination of two order parameters that measure hydrophobic lipid–membrane contacts between the transferring lipid and closest membrane leaflet. Both parameters are based on the collection of distances $d_{\mathrm{CC}}^{(i)}$ between a hydrophobic carbon of the lipid and a hydrophobic carbon of the membrane, where i labels a particular carbon-carbon (CC) pair: (1) $\min(d_{\mathrm{CC}}) = \min_i d_{CC}^{(i)}$ is the minimum of these CC distances; and (2) n_{CC} is the number of CC pairs that satisfy $d_{\mathrm{CC}}^{(i)} \leq 1$ nm. In detail,

$$r_{\mathrm{LxS}} = \alpha_1 \min(d_{\mathrm{CC}}) + \alpha_2 n_{\mathrm{CC}} + \alpha_0 \tag{1}$$

with coefficients $\alpha_1 = -2.247\ \mathrm{nm}^{-1}$, $\alpha_2 = 0.004828$, and $\alpha_0 = 0.6014$ such that r_{LxS} is a unitless quantity. During all enhanced sampling simulations, r_{LxS} was calculated using a differentiable form for $\min(d_{\mathrm{CC}})$,

$$\gamma \left[\log \left(\sum_i \exp(\gamma / d_{\mathrm{CC}}^{(i)}) \right) \right]^{-1} \tag{2}$$

with $\gamma = 200$ nm, and for n_{CC},

$$\sum_i \frac{1 - \left(\frac{d_{\mathrm{CC}}^{(i)} - d_0}{r_0}\right)^6}{1 - \left(\frac{d_{\mathrm{CC}}^{(i)} - d_0}{r_0}\right)^{12}} \tag{3}$$

with $d_0 = 1$ nm and $r_0 = 0.025$ nm. Q is calculated using the functional form developed to calculate the fraction of native protein contacts [32], specifically,

$$Q = \frac{1}{N} \sum_{(i,j)} \left[1 + \exp\left[\beta(r_{ij} - \lambda r_{ij}^{(0)})\right]\right]^{-1}, \tag{4}$$

where N is the total number of contact pairs (i, j) between an atom i of C1P and atom j of CPTP, r_{ij} is the distance between atoms i and j, $r_{ij}^{(0)}$ is a reference distance between atoms i and j, which we take to be the average distance between the atom pair in solution-phase simulations of the C1P-bound form, $\beta = 50$ nm^{-1}, and $\lambda = 1.8$. Contact pairs used to calculate Q include: (1) pairs of hydrophobic carbons of C1P and carbons of the residues that line CPTP's hydrophobic cavity (residues 10, 14, 36, 39, 40, 42, 43, 46, 48, 50, 52, 53, 57, 110, 111, 114, 117, 118, 121, 122, 146, 150, 153, 154, 158, 162, 165, 171, and 175) that have $\langle r_{ij} \rangle \leq 7.8$ Å during solution-phase simulations of the C1P-bound form of CPTP; and (2) pairs of heavy atoms of C1P's headgroup and sphingoid backbone and heavy atoms of the residues responsible for C1P recognition (residues 52, 53, 56, 60, 96−102, 106, 110, 113, 114, 146−151, 154, and 214) that have have $\langle r_{ij} \rangle \leq 5.5$ Å during solution-phase simulations of the C1P-bound form.

To calculate the free energy landscape, we performed multi-walker [33] well-tempered metadynamics simulations [34] using the PLUMED 2 patch [74] for GROMACS. A total of 20 walkers, 10 initialized from all-atom configurations of the apo form of CPTP bound to the membrane and 10 initialized from all-atom configurations of the C1P-bound form bound to the membrane, were used. Gaussian hills with $\sigma_{r_{\mathrm{LxS}}} = 0.1$ and $\sigma_Q = 0.01$ and initial heights of 2.5 kJ/mol were added by each walker every 4 ps with a bias factor of 30. To avoid pushing the system into regions with very negative values of r_{LxS}, where C1P is free in solution far away from either the membrane or CPTP, and at very large positive values of r_{LxS}, which are unphysical, harmonic wall potentials with a spring constant of 500 kJ/mol were applied at $r_{\mathrm{LxS}} = -3$ and 15. The simulation was run for 560 ns. Then, to facilitate sampling of configurations with C1P inside CPTP by walkers initialized with the apo form, and vice versa for walkers initialized with the C1P-bound form, moving restraints were applied to each walker to pull it to $(r_{\mathrm{LxS}} = -2.5, Q = 1)$, if it was initialized from the apo form, and to $(r_{\mathrm{LxS}} = 12, Q = 0)$, if it was initialized from the C1P-bound form. The moving restraint applied a harmonic bias on r_{LxS} with a spring constant of 75 kJ/mol and a harmonic bias on Q with a spring constant of 7500 kJ/mol over the course of 20 ns. During this time, no Gaussians were deposited, but the bias due to previously accumulated Gaussians was applied. Subsequently, the multi-walker well-tempered metadynamics simulation was continued for an additional 560 ns without the moving restraints. In total, the simulation was run for 1.14 μs (cumulatively 22.8 μs). Convergence was obtained after 500 ns based on the time-independent estimator of Tiwary and Parrinello [35] (S6 Fig). After discarding the data from the first 500 ns of each walker and from the time period when moving restraints were applied, a free energy landscape and profiles along r_{LxS} and Q were obtained using the time-independent free energy estimator of Tiwary and Parrinello [35]. Error bars were calculated as the standard error of the free energy estimated from two independent 310 ns blocks.

Passive C1P transport

We calculated a free energy profile along r_{LxS} for passive transport of C1P between membranes using umbrella sampling simulations [75]. Simulations were performed using two different membrane compositions that matched the membrane compositions used for simulations with both forms of CPTP. An initial bilayer of 264 POPC lipids surrounded by 3.2 nm thick slabs of solvent was built using the CHARMM-GUI Membrane Builder [76, 77]. A lipid in each leaflet was replaced with a 16:0-C1P molecule to construct a second membrane. Sodium and chloride ions were added to achieve a salt concentration of 150 mM and to fully neutralize each system. Both membranes were energy minimized and equilibrated using a two-step protocol: (1) a 250 ps simulation using the Berendsen barostat [59]; and (2) a 250 ps simulation using the Parinello-Rahman barostat [60]. All other simulation parameters matched those given above for all-atom simulations of CPTP bound to a membrane. 300 ns production runs were then performed for each bilayer. The final configuration from the simulation of the membrane composed of both POPC and 16:0-C1P was used to initialize one enhanced sampling simulation. Another initial configuration was constructed by (1) inserting a 16:0-C1P lipid randomly into the solution above the POPC membrane such that its COM was at least 3.2 nm above the COM of the membrane, (2) energy minimizing the system, and (3) equilibrating it using the two-step protocol used for the membrane only system with the addition of harmonic restraints with a force constant of 500 kJ/mol/nm^2 on the z coordinates of all heavy atoms of 16:0-C1P. Next, to generate configurations to initialize each umbrella sampling window, 20 ns steered MD simulations were performed using a harmonic bias on r_{LxS} with a spring constant of 75 kJ/mol. During one steered simulation, a tagged 16:0-C1P was pulled from $r_{\mathrm{LxS}} = 14$ to $r_{\mathrm{LxS}} = -5$ to extract it from the membrane. In the other, the 16:0-C1P was pulled from $r_{\mathrm{LxS}} = -5$ to $r_{\mathrm{LxS}} = 14$ to insert it into the membrane. A total of 66 umbrella sampling windows were simulated with equally spaced harmonic bias centers ranging from $r_{\mathrm{LxS}} = -5$ to $r_{\mathrm{LxS}} = 15$ and a spring constant of 40 kJ/mol. All windows were run for 52 ns, and the first 20 ns was discarded to account for equilibration. Data from all windows of both systems was combined with the weighted histogram analysis method (WHAM) [78] to obtain the free energy profile for passive lipid transport. Error bars were calculated as the standard error estimated from the two independent systems.

Supporting information

S1 Fig. In solution, one side of CPTP's sandwich-like structure adjusts to the presence of C1P. Root-mean-square deviation (RMSD) of each residue's Cα atom of CPTP in its apo form relative to its C1P-bound form during solution-phase all-atom simulations. After alignment of the structures to minimize the RMSD of Cα atoms of helix α6, the RMSD between each Cα in the C1P-bound and apo forms is calculated as $\mathrm{RMSD}_{\mathrm{C}\alpha}(\mathrm{C1P} - \mathrm{apo}) = \sqrt{t^{-2} \sum_{ij} (\boldsymbol{r}_{\mathrm{C1P}}(t_i) - \boldsymbol{r}_{\mathrm{apo}}(t_j))^2}$, where i and j index all t frames in each trajectory and $\boldsymbol{r}_{\mathrm{C1P}}(t)$ and $\boldsymbol{r}_{\mathrm{apo}}(t)$ are the Cα's positions in the C1P-bound and apo forms, respectively. CPTP's secondary structure is schematically illustrated above with helices represented as rectangles and unstructured loop regions as lines. The gray region highlights residues that comprise one side of CPTP's sandwich-like structure. The dashed lines indicated the average $\mathrm{RMSD}_{\mathrm{C}\alpha}(\mathrm{C1P} - \mathrm{apo})$ for helices αN and $\alpha 1 - 3$ of 4.6 Å (white region) and helices $\alpha 4, \alpha 5, \alpha 7$, and $\alpha 8$ of 3.6 Å (gray region).

S2 Fig. Membrane binding is observed in unbiased coarse-grained simulations. (A) Minimum distance between CPTP and the membrane during

coarse-grained simulations of membrane binding. (B) Configurations observed at the end of each simulation. Four independent simulations were performed for each form of CPTP. Within 2 μs, CPTP stably bound the membrane in all but one simulation of the apo form (indicated with an asterisk).

S3 Fig. Coarse-grained representations of CPTP reproduce its internal dynamics observed in all-atom simulations. Root-mean-square fluctuation (RMSF) of Cα atoms (backbone beads) of CPTP in its apo and C1P-bound forms during solution-phase all-atom (coarse-grained) simulations.

S4 Fig. Coarse-grained representations of CPTP match its structure in all-atom simulations. Root-mean-square deviation (RMSD) of Cα atoms (backbone beads) between CPTP in its apo and C1P-bound forms during solution-phase all-atom (coarse-grained) simulations and the cystral structure of CPTP in PDB 4K85. In the top row, the RMSD for residues $8 - 214$ is plotted. All other rows show the RMSD for individual helices.

S5 Fig. Conformational changes that promote opening of gating helix $\boldsymbol{\alpha 2}$, as quantified by the angles $\boldsymbol{\theta_{\alpha 2}}$ and $\boldsymbol{\phi_{\alpha 2}}$, are coupled to membrane binding. Distributions of (A) $\theta_{\alpha 2}$ and (B) $\phi_{\alpha 2}$ for apo and C1P-bound forms of CPTP both in solution-phase and membrane-bound simulations. Decreased $\theta_{\alpha 2}$ indicates opening of the helical gate created by helix $\alpha 2$, whereas increased $\phi_{\alpha 2}$ indicates opening of the helical gate.

S6 Fig. Multi-walker well-tempered metadynamics simulations converge after 500 ns. Scaled time computed from the time-dependent bias is plotted versus simulation time on a log-log scale. The dashed gray line is the linear fit after 500 ns. The slope of this line is 29, which is consistent with the bias factor of 30 used in the simulations and, thus, indicative of convergence.

S7 Fig. Many different intermediate configurations are sampled during CPTP extraction (or insertion) of C1P from (or into) a membrane. View looking into CPTP's hydrophobic cavity of example configurations from different regions of the free energy landscape outlined in Fig 7A. C1P is rendered as van der Waals spheres and colored orange. The apo form of CPTP in configuration 1 is colored dark cyan, and the C1P-bound form in configuration 12 is colored dark magenta. The black line indicates the average position of phosphate groups of membrane lipids, and the membrane's hydrophobic core is shown in gray.

Author contributions

Conceptualization: J.R.R.; Data curation: J.R.R.; Formal analysis: J.R.R.; Investigation: J.R.R.; Methodology: J.R.R., P.L.G.; Resources: J.R.R., P.L.G.; Software: J.R.R.; Supervision: P.L.G.; Visualization: J.R.R.; Writing – Original draft preparation: J.R.R.; Writing – Review & editing: J.R.R., P.L.G; Writing – Final draft review: J.R.R.

Funding

J.R.R. acknowledges funding from the National Science Foundation Graduate Research Fellowship Program under Grant No. DGE 1752814. P.L.G. was funded by the Director,

Office of Basic Energy Sciences, Office of Science, US Department of Energy under Contract DE-AC02-05CH11231, through the Chemical Sciences Division of Lawrence Berkeley National Laboratory. This work used computational resources from the Extreme Science and Engineering Discovery Environment (XSEDE), which is supported by National Science Foundation grant number ACI-1548562, from the National Energy Research Scientific Computing Center (NERSC), a U.S. Department of Energy Office of Science User Facility located at Lawrence Berkeley National Laboratory, operated under Contract No. DE-AC02-05CH11231, and from Berkeley Laboratory Research Computing. The funders had no role in study design, data collection and analysis, decision to publish, or preparation of the manuscript.

Data availability

The data that support the findings of this study are available in the manuscript and its supporting information files. Input coordinates, topologies, and parameter files in addition to equilibrium simulation trajectories are available on Zenodo: DOI 10.5281/zenodo.7067164. Analysis code is available on GitHub: https://github.com/jrurogers/cptp-analysis.

Acknowledgements

We thank David Limmer and Layne Frechette for useful comments on the manuscript.

References

1. Hannun YA, Obeid LM. Sphingolipids and their metabolism in physiology and disease. Nat Rev Mol Cell Biol. 2018;19(3):175–191.

2. Olson DK, Frohlich F, Farese RV, Walther TC. Taming the sphinx: Mechanisms of cellular sphingolipid homeostasis. Biochim Biophys Acta. 2016;1861(8):784–792.

3. Yamaji T, Hanada K. Sphingolipid metabolism and interorganellar transport: Localization of sphingolipid enzymes and lipid transfer proteins. Traffic. 2015;16(2):101–122.

4. Breslow DK. Sphingolipid homeostasis in the endoplasmic reticulum and beyond. Cold Spring Harb Perspect Biol. 2013;5(4):a013326–a013326.

5. Maceyka M, Spiegel S. Sphingolipid metabolites in inflammatory disease. Nature. 2014;510(7503):58–67.

6. Ogretmen B. Sphingolipid metabolism in cancer signalling and therapy. Nat Rev Cancer. 2018;18:33–50.

7. Samaha D, Hamdo HH, Wilde M, Prause K, Arenz C. Sphingolipid-transporting proteins as cancer therapeutic targets. Int J Mol Sci. 2019;20(14):3554.

8. Körner C, Fröhlich F. Compartmentation and functions of sphingolipids. Curr Opin Cell Biol. 2022;74:104–111.

9. Backman APE, Mattjus P. Who moves the sphinx? An overview of intracellular sphingolipid transport. Biochim Biophys Acta Mol Cell Biol Lipids. 2021;1866(11):159021.

10. Reinisch KM, Prinz WA. Mechanisms of nonvesicular lipid transport. J Cell Biol. 2021;220(3):e202012058.

11. Egea PF. Mechanisms of non-vesicular exchange of lipids at membrane contact sites: Of shuttles, tunnels and, funnels. Front Cell Dev Biol. 2021;9:784367.

12. Jackson CL, Walch L, Verbavatz JM. Lipids and their trafficking: An integral part of cellular organization. Dev Cell. 2016;39(2):139–153.

13. Lev S. Non-vesicular lipid transport by lipid-transfer proteins and beyond. Nat Rev Mol Cell Biol. 2010;11:739–750.

14. Wong LH, Gatta AT, Levine TP. Lipid transfer proteins: The lipid commute via shuttles, bridges and tubes. Nat Rev Mol Cell Biol. 2019;20(2):85–101.

15. Arana L, Gangoiti P, Ouro A, Trueba M, Gómez-Muñoz A. Ceramide and ceramide 1-phosphate in health and disease. Lipids Health Dis. 2010;9:15.

16. Simanshu DK, Kamlekar RK, Wijesinghe DS, Zou X, Zhai X, Mishra SK, et al. Non-vesicular trafficking by a ceramide-1-phosphate transfer protein regulates eicosanoids. Nature. 2013;500(7463):463–467.

17. Mishra SK, Gao YG, Deng YB, Chalfant CE, Hinchcliffe EH, Brown RE. CPTP: A sphingolipid transfer protein that regulates autophagy and inflammasome activation. Autophagy. 2018;14(5):862–879.

18. Mishra SK, Gao YG, Zou X, Stephenson DJ, Malinina L, Hinchcliffe EH, et al. Emerging roles for human glycolipid transfer protein superfamily members in the regulation of autophagy, inflammation, and cell death. Prog Lipid Res. 2020;78:101031.

19. Zhai XH, Gao YG, Mishra SK, Simanshu DK, Boldyrev IA, Benson LM, et al. Phosphatidylserine stimulates ceramide-1-phosphate (C1P) intermembrane transfer by C1P transfer proteins. J Biol Chem. 2017;292(6):2531–2541.

20. Gao YG, Zhai X, Boldyrev IA, Molotkovsky JG, Patel DJ, Malinina L, et al. Ceramide-1-phosphate transfer protein (CPTP) regulation by phosphoinositides. J Biol Chem. 2021;296:100600.

21. McLean LR, Phillips MC. Kinetics of phosphatidylcholine and lysophosphatidylcholine exchange between unilamellar vesicles. Biochemistry. 1984;23(20):4624–4630.

22. Nichols JW. Thermodynamics and kinetics of phospholipid monomer vesicle interaction. Biochemistry. 1985;24(23):6390–6398.

23. Pownall HJ, Hickson DL, Smith LC. Transport of biological lipophiles: Effect of lipophile structure. J Am Chem Soc. 1983;105(8):2440–2445.

24. Xia Y, Li M, Charubin K, Liu Y, Heberle FA, Katsaras J, et al. Effects of nanoparticle morphology and acyl chain length on spontaneous lipid transfer rates. Langmuir. 2015;31(47):12920–12928.

25. Rogers JR, Geissler PL. Breakage of hydrophobic contacts limits the rate of passive lipid exchange between membranes. J Phys Chem B. 2020;124(28):5884–5898.

26. Rogers JR, Espinoza Garcia G, Geissler PL. Membrane hydrophobicity determines the activation free energy of passive lipid transport. Biophys J. 2021;120(17):3718–3731.

27. Gao YG, McDonald J, Malinina L, Patel DJ, Brown RE. Ceramide-1-phosphate transfer protein promotes sphingolipid reorientation needed for binding during membrane interaction. J Lipid Res. 2022;63(1):100151.

28. Malinina L, Patel DJ, Brown RE. How α-helical motifs form functionally diverse lipid-binding compartments. Annu Rev Biochem. 2017;86(1):609–636.

29. Malinina L, Simanshu DK, Zhai X, Samygina VR, Kamlekar R, Kenoth R, et al. Sphingolipid transfer proteins defined by the GLTP-fold. Q Rev Biophys. 2015;48(3):281–322.

30. Brown RE, Mattjus P. Glycolipid transfer proteins. Biochim Biophys Acta Mol Cell Biol Lipids. 2007;1771(6):746–760.

31. Schmidtke P, Bidon-Chanal A, Luque FJ, Barril X. MDpocket: Open-source cavity detection and characterization on molecular dynamics trajectories. Bioinformatics. 2011;27(23):3276–3285.

32. Best RB, Hummer G, Eaton WA. Native contacts determine protein folding mechanisms in atomistic simulations. Proc Natl Acad Sci U S A. 2013;110(44):17874–17879.

33. Raiteri P, Laio A, Gervasio FL, Micheletti C, Parrinello M. Efficient reconstruction of complex free energy landscapes by multiple walkers metadynamics. J Phys Chem B. 2006;110(8):3533–3539.

34. Barducci A, Bussi G, Parrinello M. Well-tempered metadynamics: A smoothly converging and tunable free-energy method. Phys Rev Lett. 2008;100(2).

35. Tiwary P, Parrinello M. A time-independent free energy estimator for metadynamics. J Phys Chem B. 2015;119(3):736–742.

36. Pabis A, Rawle RJ, Kasson PM. Influenza hemagglutinin drives viral entry via two sequential intramembrane mechanisms. Proc Natl Acad Sci U S A. 2020;117(13):7200.

37. Holthuis JCM, Menon AK. Lipid landscapes and pipelines in membrane homeostasis. Nature. 2014;510:48–57.

38. Wong LH, Copic A, Levine TP. Advances on the transfer of lipids by lipid transfer proteins. Trends Biochem Sci. 2017;42(7):516–530.

39. Miliara X, Tatsuta T, Berry JL, Rouse SL, Solak K, Chorev DS, et al. Structural determinants of lipid specificity within Ups/PRELI lipid transfer proteins. Nat Commun. 2019;10:1130.

40. Watanabe Y, Tamura Y, Kawano S, Endo T. Structural and mechanistic insights into phospholipid transfer by Ups1–Mdm35 in mitochondria. Nat Commun. 2015;6:7922.

41. Grabon A, Orlowski A, Tripathi A, Vuorio J, Javanainen M, Rog T, et al. Dynamics and energetics of the mammalian phosphatidylinositol transfer protein phospholipid exchange cycle. J Biol Chem. 2017;292(35):14438–14455.

42. Iaea DB, Dikiy I, Kiburu I, Eliezer D, Maxfield FR. STARD4 membrane interactions and sterol binding. Biochemistry. 2015;54(30):4623–4636.

43. Kudo N, Kumagai K, Tomishige N, Yamaji T, Wakatsuki S, Nishijima M, et al. Structural basis for specific lipid recognition by CERT responsible for nonvesicular trafficking of ceramide. Proc Natl Acad Sci U S A. 2008;105(2):488–493.

44. Sugiura T, Takahashi C, Chuma Y, Fukuda M, Yamada M, Yoshida U, et al. Biophysical parameters of the Sec14 phospholipid exchange cycle. Biophys J. 2019;116(1):92–103.

45. Dong J, Du X, Wang H, Wang J, Lu C, Chen X, et al. Allosteric enhancement of ORP1-mediated cholesterol transport by PI(4,5)P2/PI(3,4)P2. Nat Commun. 2019;10:829.

46. Lipp NF, Gautier R, Magdeleine M, Renard M, Albanèse V, Čopič A, et al. An electrostatic switching mechanism to control the lipid transfer activity of Osh6p. Nat Commun. 2019;10:3926.

47. Shadan S, Holic R, Carvou N, Ee P, Li M, Murray-Rust J, et al. Dynamics of lipid transfer by phosphatidylinositol transfer proteins in cells. Traffic. 2008;9(10):1743–1756.

48. Zhang X, Xie H, Iaea D, Khelashvili G, Weinstein H, Maxfield FR. Phosphatidylinositol phosphates modulate interactions between the StarD4 sterol trafficking protein and lipid membranes. J Biol Chem. 2022;298(7):102058.

49. Abraham MJ, Murtola T, Schulz R, Páll S, Smith JC, Hess B, et al. GROMACS: High performance molecular simulations through multi-level parallelism from laptops to supercomputers. SoftwareX. 2015;1-2:19–25.

50. Klauda JB, Venable RM, Freites JA, O'Connor JW, Tobias DJ, Mondragon-Ramirez C, et al. Update of the CHARMM all-atom additive force field for lipids: Validation on six lipid types. J Phys Chem B. 2010;114(23):7830–7843.

51. MacKerell AD, Bashford D, Bellott M, Dunbrack RL, Evanseck JD, Field MJ, et al. All-atom empirical potential for molecular modeling and dynamics studies of proteins. J Phys Chem B. 1998;102(18):3586–3616.

52. Venable RM, Sodt AJ, Rogaski B, Rui H, Hatcher E, MacKerell AD, et al. CHARMM all-atom additive force field for sphingomyelin: Elucidation of hydrogen bonding and of positive curvature. Biophys J. 2014;107(1):134–145.

53. Khan HM, Souza PCT, Thallmair S, Barnoud J, de Vries AH, Marrink SJ, et al. Capturing choline-aromatics cation-pi interactions in the MARTINI force field. J Chem Theory Comput. 2020;16(4):2550–2560.

54. Yesylevskyy SO, Schafer LV, Sengupta D, Marrink SJ. Polarizable water model for the coarse-grained MARTINI force field. PLoS Comput Biol. 2010;6(6):e1000810.

55. Periole X, Cavalli M, Marrink SJ, Ceruso MA. Combining an elastic network with a coarse-grained molecular force field: Structure, dynamics, and intermolecular recognition. J Chem Theory Comput. 2009;5(9):2531–2543.

56. Marrink SJ, Risselada HJ, Yefimov S, Tieleman DP, de Vries AH. The MARTINI force field: Coarse grained model for biomolecular simulations. J Phys Chem B. 2007;111(27):7812–7824.

57. Webb B, Sali A. Comparative protein structure modeling using MODELLER. Curr Protoc Bioinform. 2016;54:5.6.1–5.6.37.

58. Fiser A, Do RKG, Sali A. Modeling of loops in protein structures. Protein Sci. 2000;9(9):1753–1773.

59. Berendsen HJC, Postma JPM, van Gunsteren WF, DiNola A, Haak JR. Molecular dynamics with coupling to an external bath. J Chem Phys. 1984;81(8):3684–3690.

60. Parrinello M, Rahman A. Polymorphic transitions in single-crystals - a new molecular-dynamics method. J Appl Phys. 1981;52(12):7182–7190.

61. Wassenaar TA, Ingólfsson HI, Böckmann RA, Tieleman DP, Marrink SJ. Computational lipidomics with insane: A versatile tool for generating custom membranes for molecular simulations. J Chem Theory Comput. 2015;11(5):2144–2155.

62. de Jong DH, Singh G, Bennett WFD, Arnarez C, Wassenaar TA, Schafer LV, et al. Improved parameters for the martini coarse-grained protein force field. J Chem Theory Comput. 2013;9:687–697.

63. Wassenaar TA, Pluhackova K, Bockmann RA, Marrink SJ, Tieleman DP. Going backward: A flexible geometric approach to reverse transformation from coarse grained to atomistic models. J Chem Theory Comput. 2014;10(2):676–690.

64. Nosé S. A molecular-dynamics method for simulations in the canonical ensemble. Mol Phys. 1984;52(2):255–268.

65. Hoover WG. Canonical dynamics - equilibrium phase-space distributions. Phys Rev A. 1985;31(3):1695–1697.

66. Hockney WR. The potential calculation and some applications. Methods Comput Phys. 1970;9:136–211.

67. Hess B, Bekker H, Berendsen HJ, Fraaije JG. Lincs: A linear constraint solver for molecular simulations. J Comput Chem. 1997;18(12):1463–1472.

68. Essmann U, Perera L, Berkowitz ML, Darden T, Lee H, Pedersen LG. A smooth particle mesh ewald method. J Chem Phys. 1995;103(19):8577–8593.

69. Páll S, Hess B. A flexible algorithm for calculating pair interactions on SIMD architectures. Comput Phys Commun. 2013;184(12):2641–2650.

70. Lingenheil M, Denschlag R, Reichold R, Tavan P. The “hot-solvent/cold-solute” problem revisited. J Chem Theory Comput. 2008;4(8):1293–306.

71. Bussi G, Donadio D, Parrinello M. Canonical sampling through velocity rescaling. J Chem Phys. 2007;126(1):014101.

72. Michaud-Agrawal N, Denning EJ, Woolf TB, Beckstein O. MDAnalysis: A toolkit for the analysis of molecular dynamics simulations. J Comput Chem. 2011;32(10):2319–2327.

73. Harris CR, Millman KJ, van der Walt SJ, Gommers R, Virtanen P, Cournapeau D, et al. Array programming with numpy. Nature. 2020;585(7825):357–362.

74. Tribello GA, Bonomi M, Branduardi D, Camilloni C, Bussi G. PLUMED 2: New feathers for an old bird. Comput Phys Commun. 2014;185(2):604–613.

75. Torrie GM, Valleau JP. Non-physical sampling distributions in monte-carlo free-energy estimation - umbrella sampling. J Comput Phys. 1977;23(2):187–199.

76. Jo S, Kim T, Iyer VG, Im W. CHARMM-GUI: A web-based graphical user interface for CHARMM. J Comput Chem. 2008;29(11):1859–1865.

77. Wu EL, Cheng X, Jo S, Rui H, Song KC, Dávila-Contreras EM, et al. CHARMM-GUI membrane builder toward realistic biological membrane simulations. J Comput Chem. 2014;35(27):1997–2004.

78. Kumar S, Bouzida D, Swendsen RH, Kollman PA, Rosenberg JM. The weighted histogram analysis method for free-energy calculations on biomolecules. 1. The method. J Comput Chem. 1992;13(8):1011–1021.